Geophysical Research Letters

RESEARCH LETTER
10.1029/2021GL095996

Dynamic Imaging of Glacier Structures at High-Resolution Using Source Localization With a Dense Seismic Array

Ugo Nanni[1,2], Philippe Roux[3], Florent Gimbert[1], and Albanne Lecointre[3]

[1]IGE, University of Grenoble Alpes, CNRS, IRD, Grenoble, France, [2]Now at Department Geosciences, University of Oslo, Oslo, Norway, [3]ISTerre, University of Grenoble Alpes, University of Savoie Mont Blanc, CNRS, IRD, IFSTTAR, Grenoble, France

Key Points:

- We present an innovative array-processing approach to image glaciers structures at high resolution by locating seismic sources
- We investigate a large range of spatial phase coherences, from very low up to very high, over narrow frequency bands and short time windows
- We image the spatial and temporal dynamics of sources originating from active and passive crevasses as well as from subglacial hydrology

Supporting Information:

Supporting Information may be found in the online version of this article.

Correspondence to:

U. Nanni,
ugo.nanni0158@gmail.com

Citation:

Nanni, U., Roux, P., Gimbert, F., & Lecointre, A. (2022). Dynamic imaging of glacier structures at high-resolution using source localization with a dense seismic array. *Geophysical Research Letters*, *49*, e2021GL095996. https://doi.org/10.1029/2021GL095996

Received 9 SEP 2021
Accepted 16 FEB 2022

Author Contributions:

Conceptualization: Philippe Roux
Formal analysis: Albanne Lecointre
Funding acquisition: Philippe Roux
Investigation: Philippe Roux, Florent Gimbert
Software: Philippe Roux, Albanne Lecointre
Supervision: Philippe Roux, Florent Gimbert
Validation: Philippe Roux
Writing – review & editing: Philippe Roux, Florent Gimbert

Abstract Dense seismic array monitoring combined with advanced processing can help retrieve and locate a variety of seismic sources with unprecedented resolution and spatial coverage. We present a methodology that goes beyond classical localization algorithms through gathering various types of sources (impulsive or continuous) using a single scheme based on a gradient-descent optimization and evaluating different levels of phase coherence. We apply our methodology on an Alpine glacier and demonstrate that we can retrieve the dynamics of active crevasses with a metric resolution using sources associated with high phase coherence; the presence of diffracting materials (e.g., rocks) trapped in transverse crevasses using sources with moderate phase coherence; and the two-dimensional time evolution of the subglacial hydrology system using sources with low phase coherence. Our study highlights the strength of using an appropriate and systematic seismological approach to image a wide range of subsurface structures and phenomena in settings with complex wavefields.

Plain Language Summary Over the past two decades, the growing use of dense seismic arrays has often overcome limitations of traditional observations methods and yielded new insights on the physics of subsurface process and properties. Yet scientific and computational challenges remain to be addressed for using the appropriate array-processing approaches and automating the techniques on large volume of data and for complex wavefields. In this paper we address such challenges in the particular case of monitoring glaciers, which host numerous and diverse sets of seismic sources that produce signals ranging from impulsive to tremor-like. We combine a physics-based and a statistical approach to explore with a dense seismic array the spatial coherence of the seismic wavefield generated by such a diversity of sources. We show that even a small coherence in the phase signal remains rich in statistical information on concomitant and/or low amplitudes micro-seismic sources. This allows us to localize seismic sources with a super-resolution (meter to decameter) and identify emerging patterns associated with a wide range of glacier features and their dynamics, ranging from active crevasses, debris in transverse passive crevasses and subglacial water flow. Such methodological and conceptual advance may enable a more efficient and complete imaging of geophysical objects.

1. Introduction

Over the past two decades, the use of dense seismic arrays has become widespread at all spatial scales in geophysics thanks to the development of low-cost autonomous and synchronized seismic sensors (Ben-Zion et al., 2015; Lin et al., 2013; Moreau et al., 2020; Shen et al., 2012). At the continental scale, arrays of several hundred or thousands of sensors (e.g., USArray, Hi-Net (Ekström et al., 2009; Okada et al., 2004)) have yielded accurate maps of phase and group velocities for surface waves in the frequency range where ocean-driven ambient seismic noise dominates (<~1 Hz). On a local scale (few to tens of kilometers), passive imaging and monitoring of the subsurface have become classical tools with the investigation of higher frequency waves (few to tens of Hz) often generated by anthropogenic noise (Pinzon-Rincon et al., 2021). Seismic exploration conducted using active sources and a number of sensors often exceeding 10 thousand has long been used for near-surface imaging purposes, particularly in the oil and gas industry (Chmiel et al., 2021; Lindseth, 1968). With the increased monitoring capabilities now affordable in academia, the scientific literature has recently been full of work that uses dense seismic arrays to image many different kinds of geophysical objects at varying spatial scales, such as active faults, volcanoes, geothermal systems, landslides, glaciers, oil exploration fields. Thanks to the remote and non-invasive nature of seismic instrumentation, the use of dense seismic arrays often allows overcome limitations of traditional observation methods and yield new insights on the physics of subsurface processes.

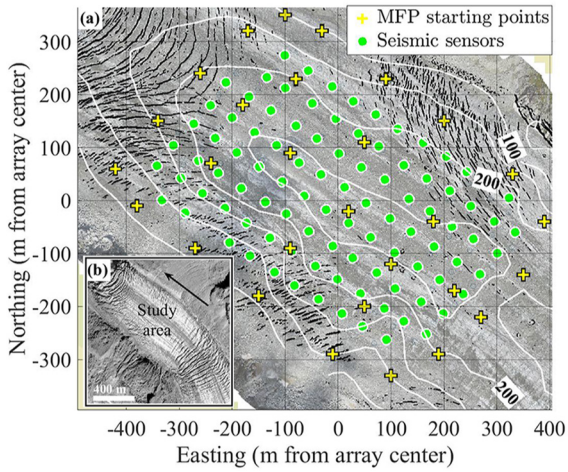

Figure 1. (a) Monitoring set-up and (b) aerial view of the Glacier d'Argentière field site (France, Mont Blanc mountain range). (a) The seismic array (green dots) is composed of 98 seismic stations with Fairfield Nodal Z-Land 3 components, which are indicated according to their positions at the beginning of the survey period. White contour lines show 50m-spaced ice thickness contours (Gimbert et al., 2021). The yellow crosses show the locations of the 29 starting points used for minimization. Glacier flows toward northwest (top left, black arrow in (b)). Aerial view provided by Bruno Jourdain. The study area is located at ∼2400 m of elevation and at 45°57'80"N 6°58'43"E.

The use of dense seismic arrays requires array-processing techniques in which one analyzes the spatial coherence of the phase associated to incident waves recorded on all or part of the array (i.e., the relative phase difference between signals at the different sensors). Although very promising, the recent development of algorithms based on artificial intelligence and neural networks with or without a learning stage (Bianco et al., 2019; Seydoux et al., 2020; Shi et al., 2021) has not yet taken the place of wave physics as an essential tool to take advantage of the spatial density of seismic arrays (Seydoux et al., 2016). Current physics-based algorithms measure the phase coherence of the seismic signal over an array via the construction of the cross-spectral density matrix (CSDM, Cros et al., 2011). This measure is then coupled to an inversion scheme (for imaging) or to a projection on a 2D/3D modeled seismic wavefield (for source localization), this last algorithm forming the fundamental principle of the widely used Matched Field Processing (MFP, see details in Section 2.2, Gresse et al., 2018; Vandemeulebrouck et al., 2013). Through a recursive matching of modeled with observed phase delays, MFP algorithms lead to the production of an "ambiguity surface" interpreted as a probabilistic estimate of the epicentral coordinate of a seismic source (Chmiel et al., 2019; Corciulo et al., 2012; Gradon et al., 2019, 2021). Applying MFP on large volumes of data and in settings where complex wavefields are observed has three main difficulties: (a) matching the appropriate model, built on the basis of a point-like source, to the measurements, (b) dealing with multiple and concomitant sources that degrades the spatial coherence of the CSDM, and (c) automating the technique within a multidimensional model space including 3D source locations and phase velocity.

In this paper, we address the above listed challenges in the specific case of monitoring glaciers, which generate numerous sources with extraordinarily diverse nature, from impulsive to tremor like signals (Podolskiy and Walter, 2016). The aim of our study is to go beyond classical localization algorithms that generally assign a source to a time window associated with high spatial phase coherence and reject time windows associated with low spatial phase coherence for which localization is considered ambiguous. We combine an efficient MFP algorithm and a statistical approach to gather the diverse range of sources into a single scheme. We show that despite the ambiguity on localization, a partial phase coherence on the array remains rich in statistical information on concomitant and/or low amplitudes micro-seismic sources. Sorting all sources by degree of phase coherence, we identify distinct patterns associated with different glacier features and their dynamics, ranging from active crevasses, debris in transverse crevasses and subglacial water flow.

2. Materials and Methods

2.1. Field Experiment

Our study lies in the context of the RESOLVE project (Gimbert et al., 2021), which consisted in the deployment of 98 seismic sensors within the ablation zone of the Argentière Glacier (French Alps, Figure 1). The array covers an area of about 650 × 800 m, with a ∼40–50 m station-interspacing. Continuous acquisitions were made during 35 days at the onset of the 2018 melt season (April-June). This area is also well documented through other local measurements (Gimbert et al., 2021), which show that glacial surface velocity was on the order of 0.1 m. day^{-1} and that subglacial water discharge increased from 0.1 m^3. sec^{-1} to 4 m^3. sec^{-1} over the study period. Geophysical imaging through ambient seismic noise correlation has already been conducted with this seismic data set as well as the identification of coherent seismic sources (icequakes) located on or near the surface (crevasses, block falls) and at the rock-glacier interface (Sergeant et al., 2020). At high frequencies ((10–20) Hz), short and repeated pulses mainly composed of surface waves (phase velocity ∼1,590 m. sec^{-1}) cross the entire array and dominate the seismic signal with a few seconds recurrence time (Gimbert et al., 2021). At low frequency ((3–7) Hz), subglacial water flow has been observed to generate continuous seismic noise (Nanni, Gimbert, Vincent

et al., 2020) and a dynamic mapping of subglacial hydrological flows was carried out via the study of spatially dispersed seismic sources generating low phase coherence (Nanni, Gimbert, et al., 2021).

2.2. Matched Field Processing

We focus here on the ground motion extracted from the vertical component. We first compute the discrete Fourier transform $d(\omega)$ of a given data vector $d(t)$ recorded by the 98 sensors over a frequency ω, and calculate the corresponding CSDM K as

$$K(\omega) = d(\omega)d^H(\omega), \tag{1}$$

where H is the Hermitian transpose. We model the synthetic wavefield from a point-like source model with a frequency-domain Green's function that has four degrees of freedom: the source spatial coordinates x, y and z and the medium homogenous phase velocity c. For a given element a of these four dimensions we model the Green's function replica vector d (ω,a)

$$d(\omega, \mathrm{a}) = \exp\left(^{i\omega r_a}/_c\right), \tag{2}$$

where r_a is the distance between each receiver and the trial source position. With this approach we thus consider spherical waves and allow locating sources close to and within the seismic array (Gimbert et al., 2021). For each time window T we search for the lowest relative difference between the observed and modeled phase delays, that is, the highest phase coherence. To do so we calculate the Bartlett processor as

$$B_{Bartlett}(\omega, \mathrm{a}) = \sum_{\omega} |d(\omega, \mathrm{a})^H K(\omega) d(\omega, \mathrm{a})|. \tag{3}$$

we refer to the $B_{Bartlett}(\omega)$ values as the MFP output. It ranges from 0 to 1 with higher values corresponding to higher phase coherence (Corciulo et al., 2012; Cros et al., 2011; Gradon et al., 2019, 2021; Gresse et al., 2018). In order to converge to the best match between the observed and the modeled phase delays, we use a gradient-based minimization algorithm that relies on the downhill simplex search method (Nelder-Mead optimization; Lagarias et al., 1999). It can occur that within a given time window T simultaneous micro-seismic sources of varying amplitudes occur, which causes wavefield superposition and a drop in the phase coherence. As a result, a large number of local minima may characterize the exploration of the model space (Chmiel et al., 2019; Gradon et al., 2021). In order to probe such minima we start the minimization algorithm from a set of 29 points covering all azimuthal directions around the targeted sources over an area of 400 × 400 m^2 centered on the array center (yellow crosses in Figure 1; Text S4 in Supporting Information S1). The originality of our approach is to keep all localizations (x, y, z, c) obtained from the 29 minimizations and to analyze these results with respect to their associated MFP output value. Such an exhaustive and systematic approach is made possible through a drastic reduction of computational cost using the gradient-based minimization algorithm instead of a multi-dimensional grid search approach.

Considering two extreme cases gives an idea of the population of source localizations we obtained. When a single icequake signal is present in a window T, the 29 minimizations converge to a single localization with an MFP output close to 1 (Gimbert et al., 2021; Sergeant et al., 2020). The accuracy of such localization is expected to be of about half the seismic wavelength λ, considering wave diffraction in the far-field (i.e., source-to-stations distances > λ; Fink et al., 2000). On the contrary, if the window T records only random noise, the 29 minimizations generate as many localizations scattered over the study area with MFP outputs of the order of 0.001 (Text S1, Figure S1 in Supporting Information S1). Between these two extremes, the case of multiple sources leads to clusters of localizations (Nanni, Gimbert, et al., 2021). The accuracy of such localizations cannot be determined for single events because of the complex wavefield generated by the concomitant overlapping sources. One should note that across frequencies, a source located with a similar MFP output is not expected to bear the same accuracy, since the phase coherence increases with increasing seismic wavelength (Rost & Thomas, 2002). For instance, a phase coherence observed by five to 10 neighboring sensors (with inter-distance ∼40 m) would lead to a MFP output around 0.05 at frequencies of about 20 Hz (λ ∼80 m) while around 0.1 at frequencies of about 10 Hz (λ ∼160 m).

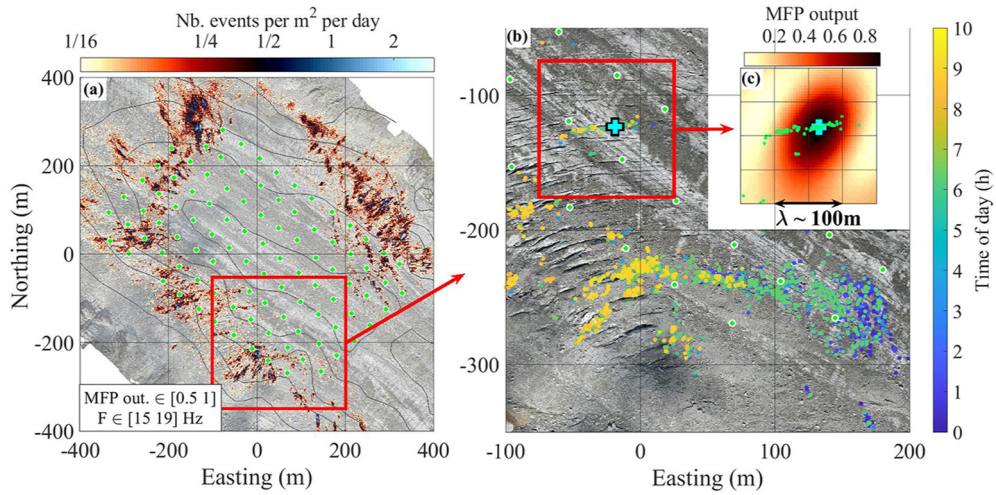

Figure 2. Two-dimensional maps of source location obtained from matched-field processing (MFP) for the 17 ± 2 Hz frequency (F) range and the (0.5–1) MFP output range. (a) Map averaged over a 30 days. The color scale shows the number of events per square meter per day. Contour lines show the 50-m-spaced ice thickness contours. Red square shows zoom of panel (b). Green dots show seismic sensors locations. (b) Source location obtained for April 25th between 0:00 and 10:00 a.m. UTC. The color scale shows the time of each event. Red square shows zoom of panel (c). (c) Diffraction-based focal spot obtained from MFP for the event identified with the green cross. The color scale shows the MFP output values. Green dots show localized seismic sources.

2.3. Statistical Analysis of Localized Sources

To build a large catalog of seismic events, we apply MFP over the entire study period using time windows of $T = 1$ s with 0.5-s overlap. We select three frequency bands of (5, 13, 17) ±2 Hz over which we coherently apply the MFP for each bin of 0.1 Hz within this range. To preserve the quality of the source localizations, we only keep sources detected within the glacier at distance less than 400 m from the seismic array center and with realistic phase velocities ((1,000–3,500) m. sec^{-1}, Nanni, Gimbert, et al., 2021; Sergeant et al., 2020). We also only keep sources with MFP output greater than a threshold of 0.01, which is one order of magnitude above the level of phase coherence associated with a random phase field. We then project all sources on the glacier's surface plane to avoid dealing with source depth, which is poorly constrained as a result of (a) the depth-vs-velocity ambiguity of the MFP due to the 2D configuration of our array and (b) the large spreading of the surface wave sensitivity kernel with depth (Gimbert et al., 2021). In order to investigate a particular range of phase coherences (Section (c), we add up all sources found within this range, which can be up to 29 per s, over a given period in each 1×1 m^2 cell of an 400×400 m^2 (x, y) grid centered on our seismic array. By doing so we build two-dimensional maps of source location density.

3. Results

3.1. Imaging Crevasse Dynamics From Impulsive Events

In Figure 2a, we show the spatial distribution of the seismic events associated with a high (global) phase coherence (MFP output (0.5–1); frequency (15–19) Hz). For these events, the convergence of the algorithm leans toward the global minimum of the relative difference between the observed and modeled phase delays, independent of the starting point (Gimbert et al., 2021). We observe that the events are mainly located on the side of the glacier, where crevasses are observed (Figures 1a and 2a) and have a relatively low occurrence rate of about 1 event per day per square meter (d^{-1}. m^{-2}). On the eastern and western flanks of the glacier where ice is thinner, the events are almost aligned orthogonally to the glacier flow, whereas on the more central part of the glacier, they tend to align along flow. Such pattern is typically expected for crevasses of narrow U-shaped valley glacier as a result of maximum extensive stresses rotating form near along flow to near perpendicular flow due to increased shearing as approaching the glacier sides (Colgan et al., 2016). In Figure 2b, we show the temporal dynamics of the events observed on April 25th between 0:00 and 10:00 a.m. UTC. Over the course of the day, the crevasses activation

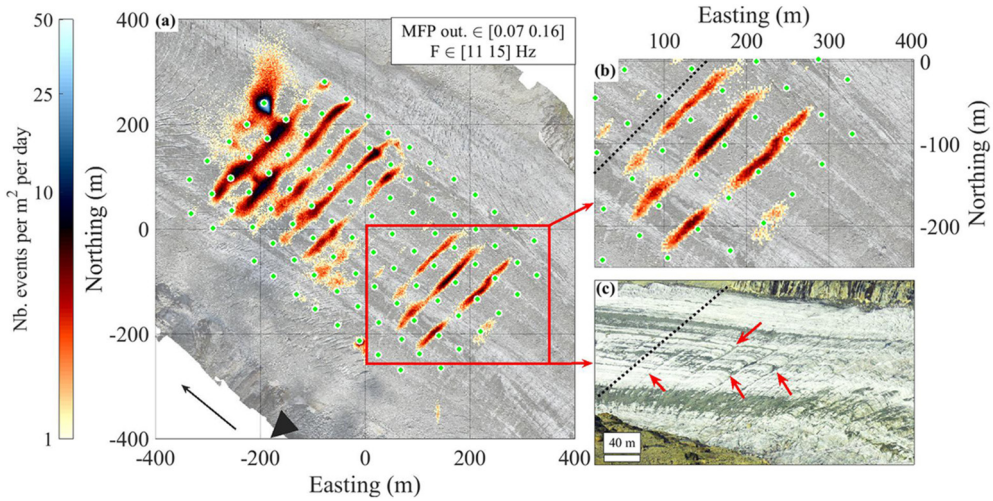

Figure 3. (a) Two-dimensional maps of the source location densities obtained for the 13 ± 2 Hz frequency (F) range and the (0.07–0.16) MFP output range averaged over a 30 days. The color scale shows the number of events per square meter per day. Black arrow shows glacier flow direction. (b) Zoom on the downglacier part of our array. Black dotted-line is orthogonal to glacier flow. (c) Helicopter view of the study area from the right flank of the glacier. Line of sight is shown in (a) with the black triangle. Red arrows show crevasses traces at the surface of the glacier. Black dotted-line is the same as in (b). Aerial view provided from Bruno Jourdain, September 2018.

migrates at a speed of about 20 m. hour^{-1}, allowing us to draw the complete geometry of the nearly 250 m-long crevasses buried under about 4 m of snow. On the eastern part of the crevasse, where the spatial spreading of the events is relatively large (∼50 m), no large crevasses are observed on the surface (Figures 1a and 2b) suggesting more diffuse and smaller structures than on the western side where clear localized structures are visible on the surface. In this western area, the geometry depicted by the successive events presents a narrow width of about or less than 5 m, which is considerably lower than λ/2 (∼45 m for a 17 Hz central frequency, Figure 2c). It thus appears that the resolution at which we are able to image crevasse geometry is higher than the accuracy expected for each individual localization (Section 2.2). This is further detailed in Figure 2c, where we observe that the focal spot obtained from a grid-search MFP conducted for the event identified with the green cross (Figures 2b and 2c) presents a much larger width (∼100 m), than the apparent resolution depicted by the events alignment along the crevasse (green dots, Figure 2c). This leads us to advance that the spread of sources on the eastern side of the crevasse (Figure 2b) is not due to localization uncertainties but reflects a real spread in the underlying source locations.

3.2. Imaging Sub-Surface Structures From Diffracted Waves

In Figure 3a, we show the spatial distribution of the seismic events associated with an intermediate phase coherence (MFP output (0.07–0.16); frequency (11–15) Hz). Due to the phase coherence being local, the relative difference between the observed and modeled phase delays present several minima and the 29 localizations obtained from the minimization algorithm are expected to be spatially dispersed. When averaged over multiple days, we observe that the spatial distribution of the localizations draws clear lines that are transverse to the glacier flow (Figure 3a). These structures are distant by about 50 m from each other, and eight of them have an average event density of around 10 days^{-1}. m^{-2}, which is an order of magnitude higher than the 1 day^{-1}. m^{-2} value previously found for crevasse sources at high coherency (Section 3. (a). We suggest that this pattern does not result from a methodological bias but rather from subsurface structures. This is supported by: (a) an inter-lines spacing little to none affected by the frequency (Figure S3 in Supporting Information S1) and (b) structures defined in a single direction while the array is clearly two-dimensional. The typical width of the transverse structures (∼10 m) remains significantly lower than λ/2 (∼60 m for a 13 Hz central frequency), which further supports our previous finding that the resolution at which we can image structures with a large group of sources is greater than the localization accuracy.

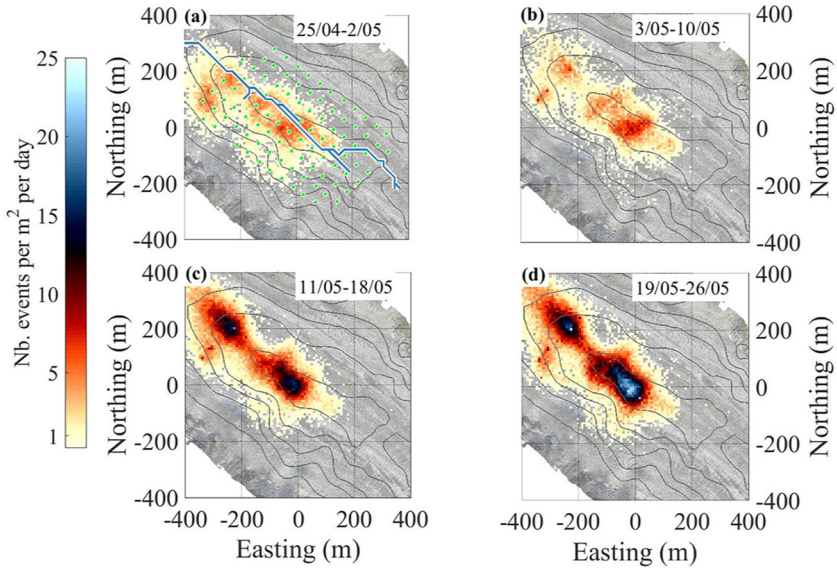

Figure 4. (a to d) Temporal evolution of the spatial patterns of the source location densities obtained for the 5 ± 2 Hz frequency range and the (0.07–0.16) MFP output range. Maps averaged over 8 days. Color scale shows the number of events per square meter per day. Contour lines show the 50-m-spaced ice thickness contours. Green dots in (a) show the seismic sensors location. The blue line in (a) shows the path that minimizes the hydraulic potential gradient calculated with a flotation fraction of 0.5 in Nanni, Gimbert, et al. (2021), which represents the likely location of subglacial waterways.

In Figure 3b, we show in more detail the downstream part of our array where four lines of events are distinguishable, as compared with Figure 3c which shows a picture of the same area taken from helicopter. In this picture, we identify 4 across-flow transverse crevasses with a geometry similar to that of the lines of events identified with seismic. Such transverse crevasses are thought to be inherited from large crevasses formed upstream (see Figure 1b) and having progressively closed as advected downstream under a more compressive stress environment (Colgan et al., 2016). Despite being small and likely inactive, we suggest that these relict crevasses create a sufficiently strong material contrast for diffracting seismic waves and our algorithm to detect diffractions as "events". Such a strong material contrast is likely permitted by the presence of fractured ice, compacted snow and/or rock debris having entered these relict crevasses when those were previously active and large (Figure S4 in Supporting Information S1).

3.3. Imaging the Subglacial Hydrology Dynamics From Low-Coherent Noise

In Figure 4, we show the spatial and temporal distribution of the seismic events associated with very low phase coherence (MFP output (0.07–0.16); frequency (3–7) Hz). These localizations are expected to be more dispersed and less reliable than in Section 3.2, because of the larger seismic wavelengths and therefore a lower phase coherence even under similar MFP output values. By summing localizations over 8-day periods we observe a characteristic pattern of sources aligning along the glacier centerline, where the ice is at maximum thickness and where hydraulic potential calculations (Figure 4a) suggest the likely location of subglacial water flow (Nanni, Gimbert, et al., 2021). These sources are studied in details in Nanni, Gimbert, et al. (2021), who showed that they are likely generated at depth near the glacier bed and are associated with subglacial water flow. The spreading of the sources in the across-flow direction (∼50 m) is smaller than λ/2 (∼150 m for a 5 Hz central frequency), and likely results from sources being distributed and/or from a reduced resolution resulting from the limited number of sensors being sensitive to a given source. The significant increase of source density from around 1 day^{-1}. m^{-2}up to 15 days^{-1}. m^{-2} that we observe over the 1 month of instrumentation is consistent with subglacial water flow discharge and associated generated seismic noise strongly increasing over the period (Nanni, Gimbert, Vincent, et al., 2020). This evolution was identified by Nanni, Gimbert, et al. (2021) as a transition from a distributed to a more localized drainage system in response to an increase in surface melt, consistent with expectations

based on numerous observational and numerical studies in different contexts (Irarrazaval et al., 2021; Lewington et al., 2020; Tranter et al., 1996; Vincent & Moreau, 2016).

4. Discussion and Conclusions

4.1. Source Location Accuracy

We observe that the horizontal resolution at which we image glaciological structures, whether they are active or inactive crevasses (Figures 2 and 3) or subglacial waterways (Figure 4), is of about λ/6 to λ/18, which is significantly higher that the accuracy of λ/2 expected for individual localizations based on far-field wave diffraction (Section 2.2; Fink et al. (2000)). We observe in Figures 2b and 2c that, by using the repetition of nearby microicequakes associated with high phase coherence, we image the geometry of crevasses with a ∼5 m resolution (∼λ/18). With such resolution we do not simply image the most localized parts of crevasses but also locations where those are more diffuse (Figure 2b). Such approach may yield key observations for the study of the mechanisms controlling the propagation of crevasses, which is a topic of important matter for the dynamics of the Greenland Ice sheet (Roeoesli et al., 2016) and the Antarctic Ice shelfs (Macayeal et al., 2019). In addition, we observe in Figures 3 and 4 that by summing over time a large number of localizations, associated with intermediate and low spatial phase coherence, allow imaging transverse crevasses with a ∼10 m resolution (∼λ/12) and the dynamics of the subglacial hydrology networks with a ∼50 m resolution (∼λ/6). This latter observation is key to understand how subglacial water flow modulates basal motion, and therefore understand the susceptibility of glaciers and ice sheets to changes in surface meltwater production due to climate change (Davison et al., 2019; Lliboutry, 1968).

We suggest that the high resolution we obtain would not have been permitted in a classical MFP framework and is made possible thanks to our fine and systematic source localization coupled to a statistical approach. Indeed, we conducted a near-field and physic-based investigation of the wavefield, which can yield single localization accuracy down to λ/8 (Pyrak-nolte et al., 1999). We then localized a very large number of sources over time, which allowed us to image structures with a resolution that can be determined by the statistical analysis of sources dispersion and not only from single localization accuracy. This shows that our protocol leads to a super-resolved imaging of glaciological structures in all respects similar to that observed in super-resolved optical imaging (Betzig et al., 2006; Hess et al., 2006; Rust et al., 2006).

4.2. Advances and Perspectives in the Investigation of Phase Coherence

The repetition and multiplication of impulse seismic sources (e.g., icequake), but also the superposition with ambient noise (e.g., of hydraulic nature), requires a more complete physical and statistical study of the recorded signal than what is traditionally done. In practice, it appears that each time window T (∼1s) contains spatially correlated information on all or part of the seismic array. Extracting this spatial phase coherence requires: (a) not to be limited to the strong MFP values classically used to confirm the detection of a microseismic source, (b) to allow MFP analysis by narrow frequency bands (here ± 2 Hz) for seismic wavelengths well sampled by the array and (c) to let the MFP algorithm explore the parameter space in search of local minima via a gradient descent technique initiated at different points inside and outside the seismic array. The novelty of our observations also lies on the diversity of the observed sources, compared to previous studies that used a similar methodological approach (Chmiel et al., 2019; Gradon et al., 2021). We observe (a) impulsive events with clear arrival time (Figure 2), (b) incoherent seismic noise generated from water turbulences (Figure 4) and (c) diffracting objects (Figure 3) that, to our knowledge, have not been observed before with a seismic source localization scheme.

The wealth of information extracted from such a complete MFP analysis is promising for the understanding of the physical processes at play in complex systems hosting a large diversity of processes that generate numerous sources, from impulsive to tremor like signals, such as glaciers, active volcanoes, landslides or active fault zones. In a time of increasing use of dense seismic arrays, our study highlights how an accurate physic-based approach can be used to image with high resolution sub-structures through localizing a variety of seismic sources. It also highlights the potential to apply a statistical and/or deep learning approach together with a physic-based approach to enhance the level of comprehension on large seismic data set.

Data Availability Statement

The codes used in this study to localize seismic sources are described and available via https://lecoinal.gricad-pages.univ-grenoble-alpes.fr/resolve/ (last access: 11/11/2021) under a creative commons attribution 4.0 international license. The data derived from the matched-field-processing (i.e., 29 sources localizations per second over 34 days and for 20 frequency bands) together with 1 day of raw seismic signal recorded over the 98 seismic stations are available via https://doi.org/10.5281/zenodo.5645545 under a creative commons attribution 4.0 international license (Nanni, Roux, et al., 2021). The complete set of raw seismic data can be found at https://doi.org/10.15778/resif.zo2018 under a creative commons attribution 4.0 international license. The complementary data associated with the dense array experiment, including the actives crevasses identification, are available via https://doi.org/10.5281/zenodo.3971815 under a creative commons attribution 4.0 international license (Nanni, Gimbert, Helmstetter, et al., 2020; Gimbert et al., 2021). The complementary data associated with the subglacial hydrology investigation (Section 3.3) are available via https://doi.org/10.5281/zenodo.4024660 under a creative commons attribution 4.0 international license (Nanni, Gimbert, Roux et al., 2020, Nanni, Gimbert et al., 2021).

Acknowledgments
The authors declare no financial conflict of interest. This work has been conducted in the framework of the RESOLVE Project (https://resolve.osug.fr/; LabEx OSUG@2020, Investissement d'avenir – ANR10LABX56 and IDEX Université Grenoble Alpes). Most of the computations presented in this paper were performed using the GRICAD infrastructure (https://gricad.univ-grenoble-alpes.fr), which is supported by Grenoble research communities, and with the CiGri tool (https://github.com/oar-team/cigri) that was developed by Gricad, Grid5000 (https://www.grid5000.fr) and LIG (https://www.liglab.fr/). FG acknowledges support from ANR SEISMORIV (ANR-17-CE01-0008) and SAUSSURE (ANR-18-CE01-0015-01). We thank Jonathan Schaeffer and David Wolyniec for support in making accessible the large data set associated to this paper. We thank Nathan Maier for making edit suggestions. We thank the two anonymous reviewers for their general and specific comments that helped improve the manuscript.

References

Ben-Zion, Y., Vernon, F. L., Ozakin, Y., Zigone, D., Ross, Z. E., Meng, H., et al. (2015). Basic data features and results from a spatially dense seismic array on the San Jacinto fault zone. *Geophysical Journal International*, *202*(1), 1–11. https://doi.org/10.1093/gji/ggv142

Betzig, E., Patterson, G. H., Sougrat, R., Lindwasser, O. W., Scott, O., Bonifacino, J. S., et al. (2006). Imaging intracellular fluorescent proteins at Nanometer resolution. *Science*, *313*(5793), 1642–1645. https://doi.org/10.1126/science.1127344

Bianco, M. J., Gerstoft, P., James, T., Ozanich, E., Roch, M. A., Gannot, S., & Deledalle, C. A. (2019). Machine learning in acoustics: Theory and applications. *Journal of the Acoustical Society of America*, *146*(5), 3590–3628. https://doi.org/10.1121/1.5133944

Chmiel, M., Roux, P., & Bardainne, T. (2019). High-sensitivity microseismic monitoring: Automatic detection and localization of subsurface noise sources using matched-field processing and dense patch arrays. *Geophysics*, *84*(6), 1–55. https://doi.org/10.1190/geo2018-0537.1

Chmiel, M., Roux, P., Wathelet, M., & Bardainne, T. (2021). Phase-velocity inversion from data-based diffraction kernels: Seismic Michelson interferometer. *Geophysical Journal International*, *224*(2), 1287–1300. https://doi.org/10.1093/gji/ggaa512

Colgan, W., Rajaram, H., Abdalati, W., McCutchan, C., Mottram, R., Moussavi, M. S., & Grigsby, S. (2016). Glacier crevasses: Observations, models, and mass balance implications. *Reviews of Geophysics*, *54*(1), 119–161. https://doi.org/10.1002/2015RG000504

Corciulo, M., Roux, P., Campillo, M., Dubucq, D., & Kuperman, W. A. (2012). Multiscale matched-field processing for noise-source localization in exploration geophysics. *Geophysics*, *77*(5), 33. https://doi.org/10.1190/geo2011-0438.1

Cros, E., Roux, P., Vandemeulebrouck, J., & Kedar, S. (2011). Locating hydrothermal acoustic sources at old faithful geyser using matched field processing. *Geophysical Journal International*, *187*(1), 385–393. https://doi.org/10.1111/j.1365-246X.2011.05147.x

Davison, B. J., Sole, A. J., Livingstone, S. J., Cowton, T. R., & Nienow, P. W. (2019). "The influence of hydrology on the dynamics of land-terminating sectors of the Greenland ice sheet". *Frontiers of Earth Science*, *7*. https://doi.org/10.3389/feart.2019.00010

Ekström, G., Abers, G. A., & Webb, S. C. (2009). Determination of surface-wave phase velocities across USArray from noise and aki's spectral formulation. *Geophysical Research Letters*, *36*(18), 5–9. https://doi.org/10.1029/2009GL039131

Fink, M., Cassereau, D., Arnaud, D., Prada, C., Roux, P., Tanter, M., et al. (2000). Time-reversed acoustics. *Reports on Progress in Physics*, *63*(12), 1933–1995. https://doi.org/10.1088/0034-4885/63/12/202

Gimbert, F., Ugo, N., Roux, P., Helmstetter, A., Garambois, S., Lecointre, A., et al. (2021). A multi-physics experiment with a temporary dense seismic array on the Argentière Glacier, French Alps: The RESOLVE project. *Seismological Research Letters*, *92*, 1185–1201. https://doi.org/10.1785/0220200280

Gradon, C., Moreau, L., Roux, P., & Ben-Zion, Y. (2019). Analysis of surface and seismic sources in dense array data with match field processing and Markov chain Monte Carlo sampling. *Geophysical Journal International*, *218*(2), 1044–1056. https://doi.org/10.1093/gji/ggz224

Gradon, C., Roux, P., Moreau, L., Lecointre, A., & Ben Zion, Y. (2021). Characterization with dense array data of seismic sources in the shallow part of the San Jacinto fault zone. *Geophysical Journal International*, *224*(2), 1133–1140. https://doi.org/10.1093/gji/ggaa411

Gresse, M., Jean, V., Byrdina, S., Chiodini, G., Roux, P., Pio Rinaldi, A., et al. (2018). Anatomy of a fumarolic system inferred from a multiphysics approach. *Scientific Reports*, *8*(1), 1–11. https://doi.org/10.1038/s41598-018-25448-y

Hess, S. T., Girirajan, T. P. K., & Mason, M. D. (2006). Ultra-high resolution imaging by fluorescence photoactivation localization microscopy. *Biophysical Journal*, *91*(11), 4258–4272. https://doi.org/10.1529/biophysj.106.091116

Irarrazaval, I., Werder, M. A., Huss, M., Herman, F., & Mariethoz, G. (2021). Determining the evolution of an Alpine glacier drainage system by solving inverse problems. *Journal of Glaciology*, *67*(263), 421–434. https://doi.org/10.1017/jog.2020.116

Lagarias, J. C., Reeds, J. A., Wright, M. H., & Wright, P. E. (1999). Convergence behavior of the Nelder-Mead simplex algorithm in low dimensions. *SIAM Journal on Optimization*, *9*, 112–147.

Lewington, E. L. M., Livingstone, S. J., Clark, C. D., Sole, A. J., & Storrar, R. D. (2020). A model for interaction between conduits and surrounding hydraulically connected distributed drainage based on geomorphological evidence from Keewatin, Canada. *The Cryosphere*, *14*(9), 2949–2976. https://doi.org/10.5194/tc-14-2949-2020

Lin, F.-C., Li, D., Clayton, R. W., & Hollis, D. (2013). High-resolution 3D shallow crustal structure in long beach, California: Application of ambient noise tomography on a dense seismic Array Noise tomography with a dense array. *Geophysics*, *78*(4), Q45–Q56. https://doi.org/10.1190/geo2012-0453.1

Lindseth, R. O. (1968). *"Seismic data inversion"*. Digital Processing of Geophysical Data-A Review (Vol. 11–12). Society of Exploration Geophysicists.

Lliboutry, L. (1968). General theory of subglacial cavitation and sliding of temperate glaciers. *Journal of Glaciology*, *7*(49), 21–58. https://doi.org/10.1017/S0022143000020396

MacAyeal, D. R., Douglas, R., Banwell, A. F., Emile, A. O., Lin, J., Willis, I. C., et al. (2019). Diurnal seismicity cycle linked to subsurface melting on an ice shelf. *Annals of Glaciology*, *60*(79), 137–157. https://doi.org/10.1017/aog.2018.29

Moreau, L., Boué, P., Serripierri, A., Weiss, J., Hollis, D., Ildut, P., et al. (2020). Sea ice thickness and elastic properties from the analysis of multimodal guided wave propagation measured with a passive seismic array. *Journal of Geophysical Research: Oceans*, *125*(4), 1–17. https://doi.org/10.1029/2019JC015709

Nanni, U., Gimbert, F., Roux, P., & Lecointre, A. (2020). DATA of 'resolving the 2D temporal evolution of subglacial water flow with dense seismic array observations. *Zenodo*. https://doi.org/10.5281/zenodo.4024660

Nanni, U., Gimbert, F., Roux, P., & Lecointre, A. (2021). "Observing the subglacial hydrology network and its dynamics with a dense seismic array". *Proceedings of the National Academy of Sciences 118* (28). https://doi.org/10.1073/pnas.2023757118

Nanni, U., Gimbert, F., Vincent, C., Gräff, D., Walter, F., Piard, L., & Moreau, L. (2020). Quantification of seasonal and diurnal dynamics of subglacial channels using seismic observations on an Alpine glacier. *The Cryosphere*, *14*(5), 1475–1496. https://doi.org/10.5194/tc-14-1475-2020

Nanni, U., Gimbert, R., Helmstetter, G., Lecointre, W., et al. (2020). *DATA of the RESOLVE project*. https://doi.org/10.5281/zenodo.3971815

Nanni, U., Roux, P., Gimbert, F., & Lecointre, A. (2021). Seismic source location with a match field processing approach during the RESOLVE dense seismic array experiment on the glacier d'Argentiere. *Zenodo*. https://doi.org/10.5281/zenodo.5645545

Okada, Y., Kasahara, K., Sadaki, H., & Obara, K. (2004). Recent progress of seismic observation networks in Japan. *Earth Planets and Space*, *56*(1), 012039. https://doi.org/10.1088/1742-6596/433/1/012039

Pinzon-Rincon, L., Lavoué, F., Mordret, A., Boué, P., Brenguier, F., Dales, P., et al. (2021). Humming trains in seismology: An opportune source for probing the shallow crust. *Seismological Society of America*, *92*, 623–635. https://doi.org/10.1785/0220200248

Podolskiy, E. A., & Walter, F. (2016). Cryoseismology. *Reviews of Geophysics*, *54*(4), 708–758. https://doi.org/10.1002/2016RG000526

Pyrak-Nolte, L. J., Laura, J., Mullenbach, B. L., Li, X., Nolte, D. D., & AbrahamGrader, S. (1999). Synthetic sediments using seismic wave transmission sample. *Geophysical Research Letters*, *26*(1), 127–130. https://doi.org/10.1029/1998gl900237

Roeoesli, C., Helmstetter, A., Walter, F., & Kissling, E. (2016). Meltwater influences on deep stick-slip ice quakes near the base of the Greenland ice sheet. *Journal of Geophysical Research F: Earth Surface*, *121*(2), 223–240. https://doi.org/10.1002/2015JF003601

Rost, S., & Thomas, C. (2002). Array seismology: Methods and applications. *Reviews of Geophysics*, *40*(3), 2-1–2-27. https://doi.org/10.1029/2000RG000100

Rust, M. J., Bates, M., & Zhuang, X. (2006). Sub-diffraction-limit imaging by stochastic optical reconstruction microscopy (STORM). *Nature Methods*, *3*(10), 793–796. https://doi.org/10.1038/nmeth929

Sergeant, A., Chmiel, M., Lindner, F., Walter, F., Roux, P., Chaput, J., et al. (2020). On the Green's function emergence from interferometry of seismic wave fields generated in high-melt glaciers: Implications for passive imaging and monitoring. *The Cryosphere*, *14*(3), 1139–1171. https://doi.org/10.5194/tc-14-1139-2020

Seydoux, L., Balestriero, R., Poli, P., De Hoop, M., Campillo, M., & Baraniuk, R. (2020). Clustering earthquake signals and background noises in continuous seismic data with unsupervised deep learning. *Nature Communications*, *11*(1), 1–12. https://doi.org/10.1038/s41467-020-17841-x

Seydoux, L., Shapiro, N. M., de Rosny, J., & Landès, M. (2016). Spatial coherence of the seismic wavefield continuously recorded by the USArray. *Geophysical Research Letters*, *43*(18), 9644–9652. https://doi.org/10.1002/2016GL070320

Shen, Y., Ren, Y., Gao, H., Savage, B., Stockwell, R. G., Stehly, L., et al. (2012). Journal of geophysical research: Solid earth body wave extraction and tomography at long beach, California, with ambient-noise interferometry. *Geophysical Journal International*, *120*(8–9), 1159–1173. https://doi.org/10.1002/2015JB011870

Shi, P., Seydoux, L., & Poli, P. (2021). Unsupervised learning of seismic wavefield features: Clustering continuous array seismic data during the 2009 L'Aquila earthquake. *Journal of Geophysical Research: Solid Earth*, *126*(1), e2020JB020506. https://doi.org/10.1029/2020JB020506

Tranter, M., Brown, G. H., Hodson, A. J., & Gurnell, A. M. (1996). Hydrochemistry as an indicator of subglacial drainage system structure: A comparison of alpine and sub-polar environments. *Hydrological Processes*, *10*(4), 541–556. https://doi.org/10.1002/(sici)1099-1085(199604)10:4<541::aid-hyp391>3.0.co;2-9

Vandemeulebrouck, J., Roux, P., & Cros, E. (2013). The plumbing of old faithful geyser revealed by hydrothermal tremor. *Geophysical Research Letters*, *40*(10), 1989–1993. https://doi.org/10.1002/grl.50422

Vincent, C., & Moreau, L. (2016). Sliding velocity fluctuations and subglacial hydrology over the last two decades on Argentière Glacier, Mont Blanc area. *Journal of Glaciology*, *62*(235), 805–815. https://doi.org/10.1017/jog.2016.35